

Inpainting of Ring Artifacts on Microtomographic Images by 3D CNN

Anton Kornilov*[†], Ilia Safonov*[†], Ivan Yakimchuk*

*Schlumberger Moscow Research, Moscow, Russia

[†]National Research Nuclear University MEPhI, Moscow, Russia

kranton94@mail.ru, {isafonov, iyakimchuk}@slb.com

Abstract—Ring artifacts are inevitable in microtomographic images. In a Digital Rock workflow, such defects might affect the subsequent segmentation and flow simulation. We propose a correction of ring artifacts in reconstructed microtomographic images by inpainting. Our blind inpainting method uses a 3D convolutional network U-net. For the creation of training and validation datasets, we suggest an algorithm for transferring real ring artifacts to an arbitrary place in the undistorted slices of 8 big images of sandstones and sand. The parameters of the deep neural network and loss functions are analyzed. A loss function based on the multi-scale structural similarity index (MS-SSIM) allows to achieve the best performance. The developed solution corrects ring artifacts perfectly from a point of view of visual assessment and outperforms existing inpainting methods according to quality metrics based on MS-SSIM and mean absolute error (MAE).

I. INTRODUCTION

X-ray computed microtomography (microCT) [1] is widely used for the creation of a digital twin of various solid and granular materials [2], [3] in a Digital Rock (DR) physics. This technology is applied for the estimation of reservoir characteristics in the oil and gas industry [4]. Adequacy and accuracy of such digital model depend on microCT image quality. There are numerous artifacts in reconstructed 3D microCT images [5]. Ring (circular) artifacts are very troublesome in flat-panel spiral microCT since those defects not only degrade visual quality but might effect on subsequent image segmentation and flow simulation.

Miscalibrated or defective detector elements create visible rings centered on the center of slices of a 3D image. Several techniques for mitigation of ring artifacts were developed by manufacturers of microCT systems, for example, random movement between acquisitions of adjacent shadow projections; filtering of shadow projections or sinograms before reconstructions; modification of reconstruction procedure by adding a regularization. A combination of these approaches allows to suppress the majority of considered artifacts.

Nevertheless, part of ring artifacts remains anyway and deteriorates a reconstructed image. Such artifacts look like bright and/or dark scratch-like segments of rings centered on the center of some slices. The leftmost image in Fig. 1 demonstrates examples of ring artifacts. The biggest number of the remaining rings is located in a single slice, but others deteriorate several adjacent slices. In general, an exterior of

ring artifacts for images acquired by different microCT systems is similar, but it can have small specificity.

There are several algorithms for reduction of ring artifacts on a reconstructed image [6], [7], [8], [9]. However, all those approaches have shortcomings and limitations [10]. The effectiveness of those methods greatly depends on their parameters, to achieve acceptable results adjusting the parameters from image to image is required. Since each of these algorithms assumes that ring artifacts are located on circles with a center located in the center of the slice, they have no way to eliminate artifacts on the arbitrary image fragment. The filtering modifies the entire image, not just areas damaged by ring artifacts. As a rule, existing approaches process each slice of a 3D image separately without the use of data from adjacent slices. So, local correction of ring artifacts on arbitrary 3D fragments of reconstructed microCT images remains an unsolved and topical problem.

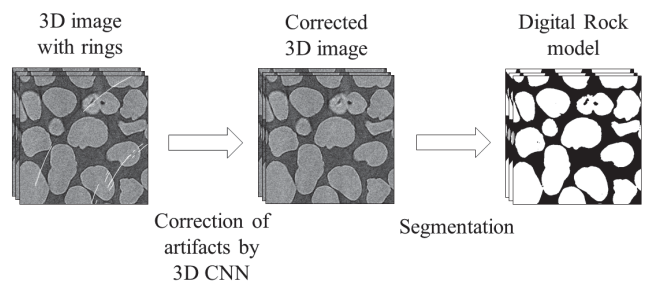


Fig. 1. Processing of images affected by ring artifacts in DR model construction workflow

We propose to include correction of ring artifacts to DR model construction workflow (see Fig. 1). It makes sense to do the correction of such local artifacts by inpainting [11]. Image inpainting is a process of restoring missing or damaged areas of an image. Deep learning allows to achieve breakthrough results in the many tasks of computer vision including inpainting. In this paper, we propose a solution for the inpainting of ring artifacts by a 3D convolutional neural network (CNN). Our aim is to develop end-to-end network for inpainting, that is without intermediate segmentation of regions damaged by rings. The biggest obstacle to train an efficient machine-learning-based model for that problem is the absence of ground truth data. To create the training and validation datasets, we suggest the method of transferring of ring artifacts from one slice to another one and between different images. In addition, our

approach for forming of validation dataset allows to assess the performance of inpainting methods by comparison of the corrected image with its undistorted reference.

This paper is organized as follows: existing deep-learning-based inpainting solutions are analyzed in Section II; in Section III we describe the creation of our training and validation datasets; the description of neural networks architecture, parameters and training strategy can be found in Section IV; in Section V we describe performance metrics and demonstrate results; and Section VI contains conclusions.

II. RELATED WORK

The research in inpainting has been very active over the recent two decades and has many applications: restoring images from scratches or text overlays, loss concealment in a context of impaired image transmission, object removal in the context of editing, or in image-based rendering [12]. Image inpainting methods can be divided into two categories: non-blind techniques and blind ones. In the first category, the regions that need to be restored are provided to the algorithm, whereas in the second no information about the locations of the corrupted areas is given and the algorithm automatically identifies the regions for inpainting [13].

Nowadays, deep-learning-based approaches achieve state-of-the-art results in inpainting. There are plenty of image inpainting methods by means of CNN [14], [15], [16], [17], [18], [19], [20], [21], [22]. The majority of analyzed publications describes generative adversarial networks (GAN) [14], [15] or various modifications of 2D U-net [23]. Neural networks in papers [14], [15], [16], [17], [18] and [19] are intended for non-blind inpainting of large regions in natural photos. For training, photos from ImageNet were used.

We don't have prior information about ring artifacts locations, so, in the first turn, we are interested in blind inpainting methods. Papers [20], [21], [22] describe blind inpainting methods for problems that are closer to our one. For training conventional U-net [23] neural network all these methods created the training sets by adding synthetic scratch-like artifacts and noises to the following types of images: fingerprints [20], coronary angiograms [21], and lunar surface images [22]. For the network training, these approaches apply the following loss functions: mean squared error [21], [22]; the sum of mean absolute error and multi-scale structural similarity index [20].

The recent publication [24] devotes almost the same problem as ours namely the reduction of ring artifacts on medical images of computed tomography (CT). That paper describes the hybrid method based on a fusion of two reconstructed images, where one image was reconstructed from sinograms processed by wavelet-Fourier filtering [25] and another image is the output of CNN, which employs as the input two images, which are reconstructed from the affected by rings sinograms and the filtered [25] ones accordingly. For dataset creation 10 full-dose clinical CT images of the patient cases from "the 2016 Low-dose CT Grand Challenge" [26] were used. The reference artifact-free sinograms and sinograms with simulated rings were obtained by forward projection. The

2D CNN has 5 convolution layers and processes 64×64 patches from a slice of 3D CT image. It is more reasonable to use a 3D CNN for correction because adjacent slices of slice damaged by ring artifact contain valuable information for correction.

III. DATASETS CREATION

Creation of big enough and the representative dataset is key for the success of techniques based on supervised learning. For training end-to-end neural network aimed for inpainting, we need corresponding to each other pairs of fragments of images: undistorted and damaged by rings. Majority of existing methods for blind inpainting of local defects by neural network generated dataset by adding pure synthetic artifacts to undistorted images. However, the appearance of ring artifacts has a big diversity. It is not just black or white scratches. We propose to transfer real artifacts from one slice to another and across images.

A. Considered MicroCT images

For processing, we got 8 reconstructed 3D images of sandstones and sand. The samples belong to 5 types: Buff Berea sandstone (BB), Bentheimer sandstone (BHI), Fontainebleau sandstone (FB), Gravelite sandstone (GRV), and Unifrac sand (UFS). We scanned the samples using Bruker SkyScan 1172 microCT system. A detailed description of the samples and enumeration of image acquisition parameters can be found in [3]. Fig. 2 shows 1 mm^2 fragments of slices from images under analysis: BB (Fig. 2a), BHI (Fig. 2b), FB (Fig. 2c), GRV (Fig. 2d) and UFS (Fig. 2e). Each 3D image has size $3968 \times 3968 \times 1840$ voxels with bit depth 8 bits per voxel.

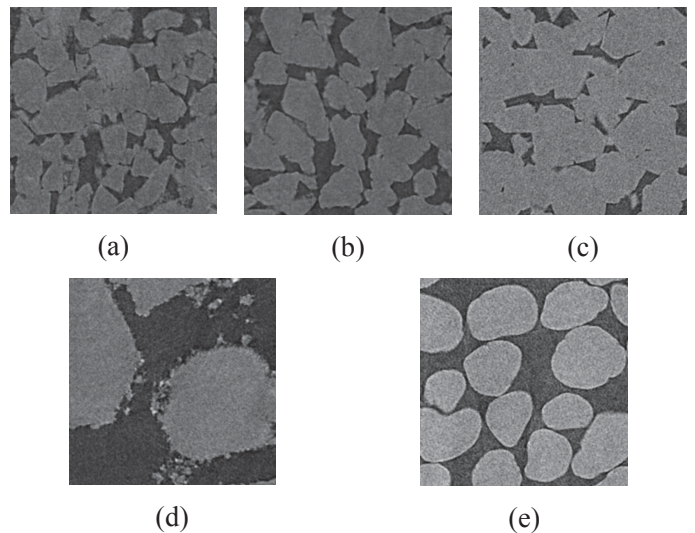


Fig. 2. 1 mm^2 fragments of microCT slices: (a) BB; (b) BHI; (c) FB; (d) GRV; (e) UFS

We made segmentation of ring artifacts regions on 14700 slices of these 8 microCT images by means of the algorithm developed earlier [27]. Briefly, the algorithm works as follows. The segmentation method transforms a slice to polar coordinates, where rings are vertical line segments. A matched filter emphasizes such vertical lines. The thresholding of the outcome of the filter marks pixels of rings. Morphological dilation with vertically-oriented structure element merges

neighboring regions. Finally, small-sized connected regions are suppressed. In general, this segmentation algorithm works well, however, the method is inapplicable for an arbitrary fragment of microCT image and it requires thorough manual selection of the following parameters for each individual image: a kernel of the matched filter, threshold, structure element of a morphological operator, and length of the least region considered as a ring.

The total number of connected regions containing ring artifacts on all these slices is about 1500. Theoretically, we are able to re-reconstruct microCT images from shadow projection with other parameters to obtain corresponding undistorted fragments, but in any case, 1500 pairs are not enough for the training of a deep network. For curiosity, we trained conventional 2D U-net for segmentation of ring artifacts, however, results were unacceptable.

B. Ring artifacts transferring algorithm

The rectangular regions containing real artifacts and corresponding masks in polar coordinates form the so-called artifacts set. Fig. 3 shows examples of ring artifacts and corresponding masks from this set. Masks are used in the validation procedure. We propose to make multifold random fusions of these rectangles with real artifacts and undistorted slices of available 8 microCT images. Our approach allows to create a big dataset with artifacts, that look visually very similar to real ones.

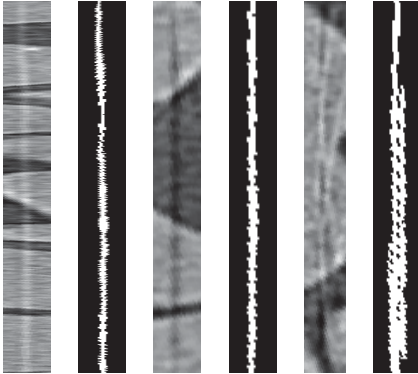


Fig. 3. Examples of artifacts and corresponding masks from the ring artifacts dataset

A ring artifact can deteriorate not only a single slice. Orthogonally to a slice plane, we computed the ring artifacts thickness for each microCT image. The distribution of thickness is presented in Fig. 4. One can see, majority of artifacts deteriorate single slice, but artifacts with thickness from 2 to 7 slices also exist. We estimated this thickness distribution as half-normal with standard deviation $\sigma = 2.3$. We transfer rings from the artifacts set to several adjacent slices, where the number of slices is randomly chosen from this distribution.

For transferring the artifact from the set to the undistorted slice of an image we propose the following approach. On slice in polar coordinates I^p , we add region with artifact I_a with the

starting point (r_a, c_a) :

$$I_{ringed}^p(r, c) = \begin{cases} I^p(r, c) + \Delta_a(r - r_a, c - c_a) : r \in [r_a, r_a + N_a] \wedge \\ c \in [c_a, c_a + M_a] \\ I^p(r, c) : otherwise \end{cases} \quad (1)$$

where (r, c) – the coordinates of slice pixel; $r = 0 \dots N-1$, $c = 0 \dots M-1$; N, N_a – the rows number of slice and rectangular region with artifact accordingly; M, M_a – the columns number of slice and rectangular region with artifact accordingly; (r_a, c_a) – the coordinates for placing of the artifact; Δ_a – the image with size $N_a \times M_a$, where each row is difference between averaged along columns k , rows of I_a and the median value of this averaged row:

$$\begin{aligned} \Delta_a(r, c) &= \mu(r, c) - \text{median}_c[\mu(r, c)], \\ \mu(r, c) &= E[I_a(r, c), I_a(r+1, c), \dots, I_a(r+k_r, c)], \end{aligned} \quad (2)$$

where $r = 0 \dots N_a-1$, $c = 0 \dots M_a-1$; $E[\bullet]$ – mean value operator; $\text{median}_c[\bullet]$ – the median in averaged row. Also, we clip pixels values of I_{ringed}^p to $[0, 255]$ range.

The artifact for addition is selected randomly from the set. On each initially undistorted slice we add 100 artifacts with r_a chosen randomly from the range $[0, N-N_a]$ and c_a from the range $[200, M]$. Because each ring can occupy several slices, we transfer an artifact with identical (r_a, c_a) on several adjacent slices. The number of slices is chosen randomly from the half-normal distribution with σ . After the addition of the artifacts to slices in polar coordinates, the image is converted back to the cartesian coordinate system. Placing a rectangle containing artifact to arbitrary place in polar coordinates automatically leads to the scaling size of the artifact in a slice in the cartesian coordinate system. Fig. 5 shows the fragment with transferred ring artifacts.

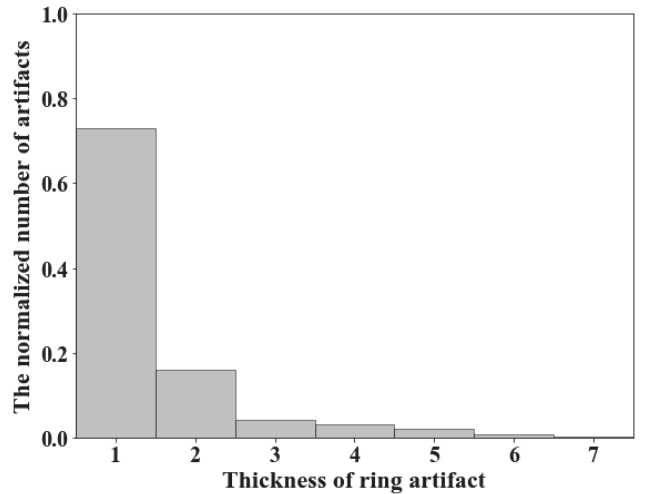


Fig. 4. Histogram of the thickness of rings

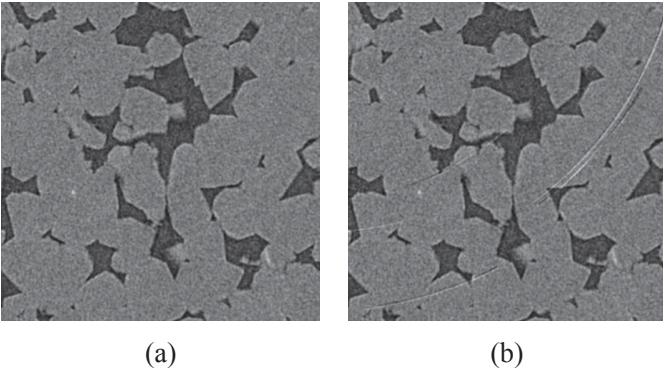


Fig. 5. Example of ring artifacts transferring: (a) fragment of slice; (b) the fragment with transferred artifacts

C. Forming of training and validation datasets

The artifacts set was divided into two non-overlapping parts: intended for training and validation. For training, we use 85% of artifacts from the set and for validation other 15%. The artifacts intended for training we place on initially undistorted slices of 7 images of sandstones (BB, BHI, FB, and GRV types). The total number of regions with artifacts in the training set is about half a million.

To estimate generalization capability, for validation we selected image of sand (UFS type), because it strongly differs from images of sandstones in training set. We add artifacts intended for validation to UFS image. The total number of regions with artifacts in the validation set is about 70000. So, there are no intersections in both images and samples of artifacts for training and validation.

IV. OUR CONVOLUTIONAL NEURAL NETWORK

Based on literature analysis and our preliminary experiments we decided to use 3D U-net [28] with patches in a

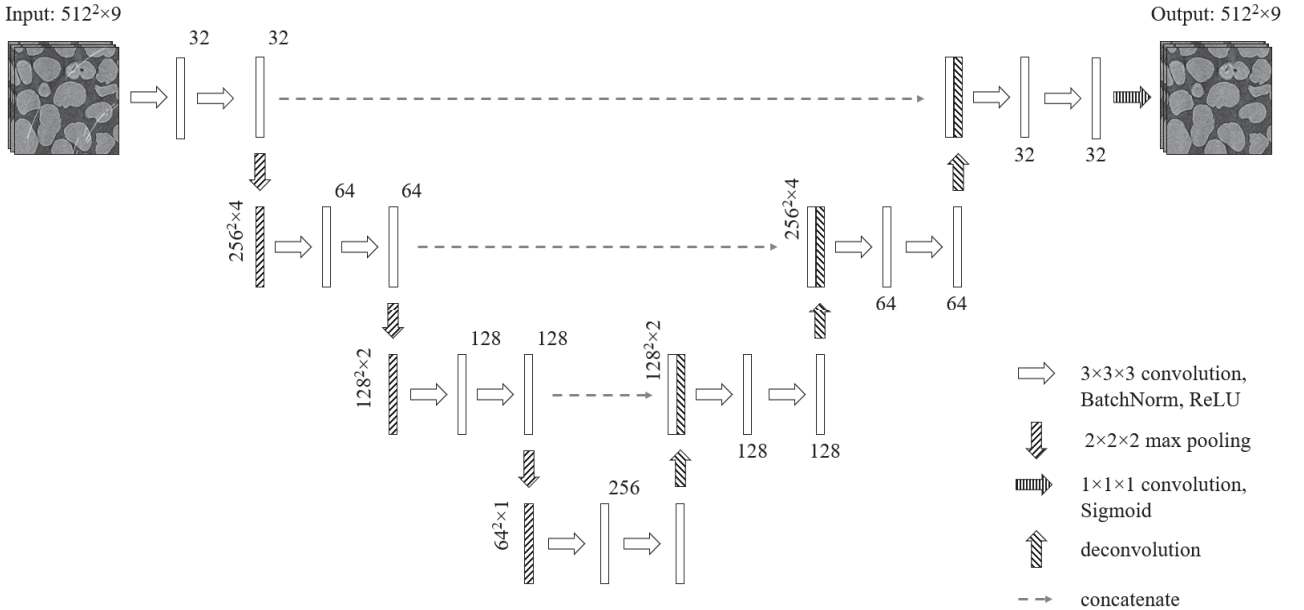


Fig. 7. The scheme of our 3D U-net

parallelepiped shape. We don't use cubic patches since one real ring artifact, as we estimated, usually occupy only from 1 to 7 consecutive slices, and because larger patches require too much GPU memory. Since rock samples do not occupy the entire image volume, we find a region of interest (ROI) that belongs to the sample. The algorithm for automatic ROI selection can be found in [27]. Fig. 6 shows an example of ROI for a slice of the UFS sample. For training and for validation we use non-overlapping $512 \times 512 \times 9$ patches, that locate inside ROI more than 80%. Fig. 7 presents the scheme of our neural network.

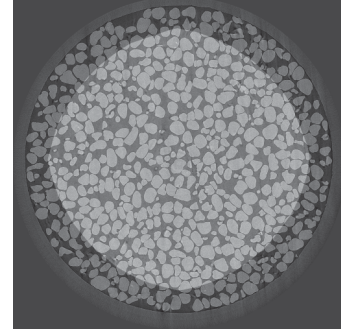


Fig. 6. Example of slice with highlighted ROI

The selection of adequate loss function is crucial for obtaining a proper model. We analyze an application of conventional mean-squared-error (MSE) loss L_{MSE} , loss function based on multi-scale structural similarity index normalized to a range from 0 to 1 (MS-SSIM) (3) [29], and the weighted sum of this loss and mean absolute error (MAE) (4). According to the review in [30], two last loss functions provide the best results in image restoration by deep neural networks.

$$L_{MS-SSIM} = 1 - MS-SSIM, \quad (3)$$

$$L_{MS-SSIM,MAE} = (1-\omega)L_{MS-SSIM} + \omega L_{MAE}. \quad (4)$$

We train our network with these three losses between patches with transferred rings and corresponded patches from reference images without rings. Usually, MS-SSIM is computed over 5 scales. We compute MS-SSIM over 3 scales with $3 \times 3 \times 3$ window because of our patch size. For $L_{MS-SSIM,MAE}$ loss we empirically estimated the value $\omega = 0.8$.

As an optimization algorithm, Adam [31] is applied with an initial learning rate 10^{-3} . Batch size equals 1. Every 100 iterations we evaluate MS-SSIM of random 50 patches from validation image and when the difference between previous and current evaluations becomes smaller 10^{-4} we stop training.

V. RESULTS

A. Performance metrics

The comprehensive review of full-reference image quality metrics [32] demonstrates metrics based on structural similarity index have the highest correlation with assessments by a human. That is why our main performance measure is based on MS-SSIM. We compute the mean value of MS-SSIM for non-overlapping $512 \times 512 \times 9$ patches. Identically to the calculation of loss function, MS-SSIM is computed for 3 scales. The best inpainting algorithm provides the highest MS-SSIM.

In addition, we calculate normalized mean absolute error separately for regions without artifact (MAE_{wr}) and with ring artifacts (MAE_r). In the ideal case, MAE_{wr} should be zero. However, it is hard to achieve for blind inpainting.

The best inpainting method has both the lowest MAE_{wr} and MAE_r . Table I contains baseline metrics for the image from the validation dataset. Developed inpainting technique should improve those figures.

B. Analysis of different loss functions

Table II contains the results for networks trained with different loss functions. It should not surprise anyone those metrics differ only in the second or third decimal place. It is explained by the small area of regions corrupted by ring artifacts relative to the area of the whole image. One can see, network trained with MSE loss performs worse than others. The network trained with $L_{MS-SSIM}$ loss achieves the best result. By visual comparison of patches processed by evaluated networks (see the outlined regions in Fig. 8), we can see that some artifacts remain on the results of networks trained with L_{MSE} and $L_{MS-SSIM,MAE}$ losses. According to visual assessment, the network trained with L_{MSE} blurs some details of the image. It is not perfect that MAE_{wr} for network trained with $L_{MS-SSIM}$ differs from zero, however visually we do not see any unwanted alterations outside of ring artifacts regions.

C. Comparison with existing inpainting algorithms

We evaluated the performance of the following non-blind inpainting algorithms, that able to process 2D slices: classical Telea's technique based on the fast marching method [11]; Liu's inpainting based on U-net with partial convolutions [17]. As the methods are non-blind, we pass masks of artifacts to their inputs.

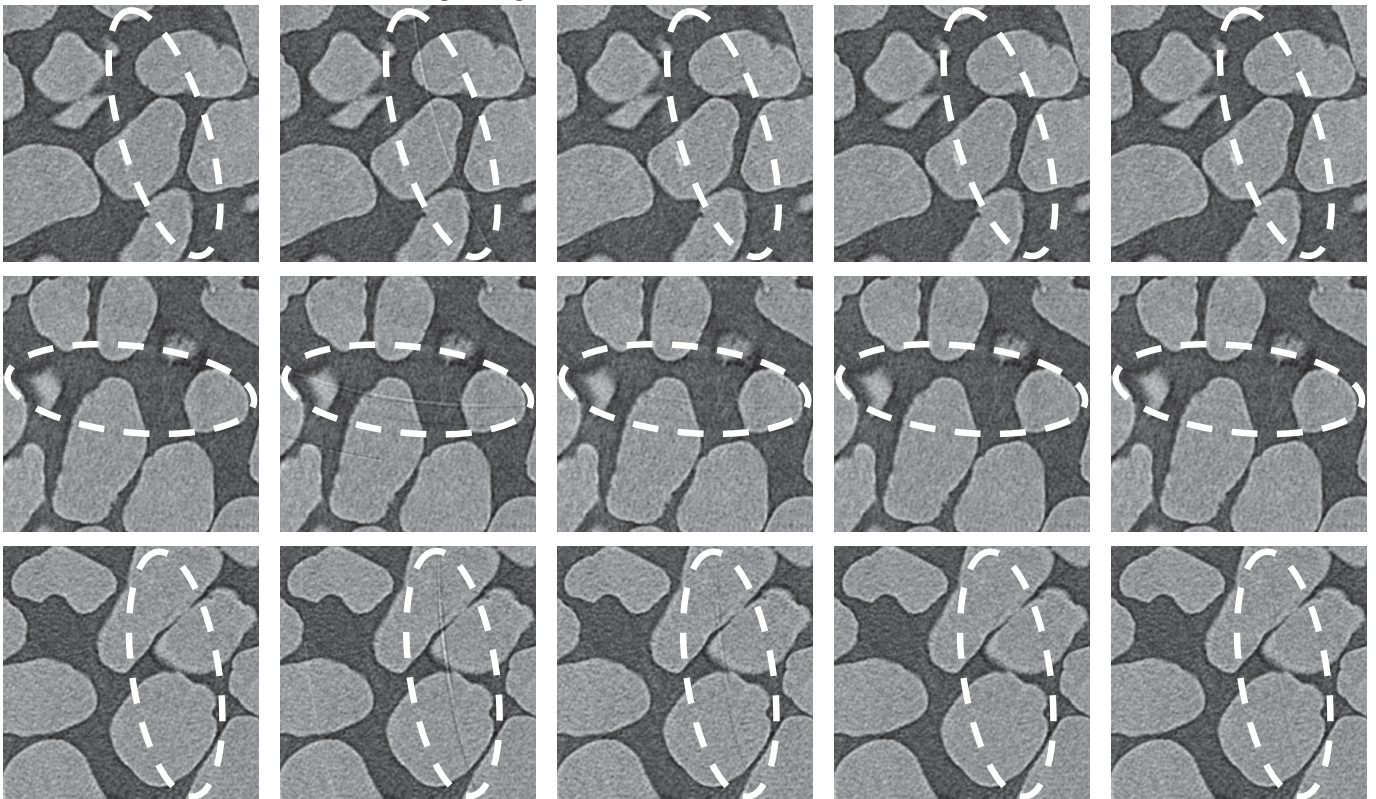


Fig. 8. Comparison of processed patches fragments: originals (first column); with transferred artifacts (second column); processed by CNN trained with L_{MSE} (third column); processed by CNN trained with $L_{MS-SSIM}$ (fourth column); processed by CNN trained with $L_{MS-SSIM,MAE}$ (fifth column)

TABLE I. PERFORMANCE METRICS BETWEEN REFERENCE IMAGE AND IMAGE WITH TRANSFERRED ARTIFACTS

MS-SSIM	MAE_{wr}	MAE_r
0.9954	0	0.053

TABLE II. PERFORMANCE METRICS OF OUR CNNs TRAINED WITH DIFFERENT LOSS FUNCTIONS

Loss function	MS-SSIM	MAE_{wr}	MAE_r
L_{MSE}	0.9913	0.013	0.025
$L_{MS-SSIM}$	0.9991	0.004	0.010
$L_{MS-SSIM,MAE}$	0.9977	0.005	0.018

TABLE III. PERFORMANCE METRICS OF NON-BLIND ALGORITHMS

Algorithm	MS-SSIM	MAE_{wr}	MAE_r
Telea [11]	0.9974	0	0.155
Ready-for-use CNN Liu et al. [17]	0.9820	0.006	0.133
Re-trained CNN Liu et al. [17]	0.9980	0.003	0.023

Table III contains the results for three non-blind methods: Telea’s technique, Liu’s model preliminary trained on ImageNet dataset, Liu’s model re-trained on microCT images. Telea’s technique has better MS-SSIM than our network trained with L_{MSE} and comparable MS-SSIM with the result of CNN trained with $L_{MS-SSIM,MAE}$. However, its MAE_r is much worse and retouching is noticeable. Our network trained with $L_{MS-SSIM}$ loss outperforms Telea’s algorithm and our solution doesn’t require masks of artifacts.

Not surprising, that the neural network preliminary trained on ImageNet dataset containing natural photos (we downloaded the ready-for-use model from <https://github.com/MathiasGruber/PConv-Keras>) shows the worst result, because photos from the training set are too far from microCT images of rock samples. Moreover, this network visually deteriorates images. Though this is the non-blind algorithm, its MAE_{wr} is not zero, because it changes a small number of pixels around the mask.

Transfer learning provides an opportunity to improve outcomes in a new task by knowledge transferring from a related task that has already been learned [33]. So, we freeze parameters of the first half of U-net pretrained on ImageNet and make training second half with the proposed loss [17]. On input we pass 512×512 patches of slices from the training dataset, corresponded masks, and ground truth patches. We perform training with suggested initial learning rate $2 \cdot 10^{-4}$ of Adam optimizer [17]. We used identical stopping criterion as for our blind CNNs. It took one day for training. As we expected, the re-trained network shows better results than the ready-for-use model. It outperforms Telea’s technique, our network trained with L_{MSE} and comparable with CNN trained with $L_{MS-SSIM,MAE}$. Nevertheless, our neural network trained with $L_{MS-SSIM}$ remains the best according to performance metrics, except MAE_{wr} , since it is a blind algorithm.

Examples of inpainting for the fragment from the first row of Fig. 8 by means of these algorithms are presented in Fig. 9.

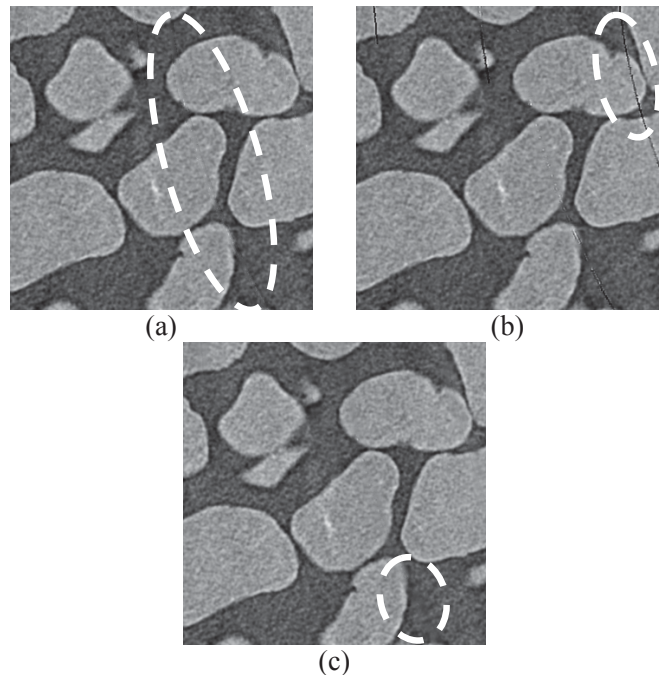


Fig. 9. Example of ring artifacts inpainting via non-blind methods: (a) Telea’s technique; (b) ready-for-use and (c) re-trained CNNs based on Liu et al. partial convolutions

D. Testing on real ring artifacts

Obviously, we have no ground truth for areas damaged by real ring artifacts. We are unable to calculate numerical performance metrics for the inpainting of slices damaged by real rings. However, the quality of correction can be done by visual assessment. We claim methods under consideration achieve similar performance for real artifacts as for transferred ones. We obtained the best result by means of CNN trained with $L_{MS-SSIM}$ loss function. The non-blind algorithms perform worse than this CNN and comparable with networks trained with L_{MSE} and $L_{MS-SSIM,MAE}$ losses.

E. Processing time

All experiments were performed on a system with two GeForce GTX 1080 Ti GPUs. GPU provides 3584 stream cores, 11 GB of memory, and 11.3 Tflops of peak single precision performance. CNN was implemented via PyTorch 1.3.0 [34]. Training time for every model was about 24 hours. Inference takes about 9 s for one $2500 \times 2500 \times 9$ fragment of image and about 200 s for the entire 3D microCT image. Such fast processing speed is more than acceptable.

VI. CONCLUSION

We proposed the algorithm for blind inpainting of ring artifacts on microCT images of various solid and granular materials. Our solution uses end-to-end 3D U-net with patches in parallelepiped shape and loss function based on MS-SSIM. The trained network provides good numerical and qualitative results. The inference stage is fast enough. Our model has high generalization capability because was validated on images and artifacts, that were not used in training. The key success factor was the preparation of big and representative dataset by means

of random placement of real ring artifacts from affected slices to undistorted ones across 3D microCT images. Procedure for artifacts and slices fusion takes into account the measured distribution of thickness of real rings.

There is room for improvement, for example, the procedure of transfer of rings to undistorted slices can be done in a true 3D manner. In the current implementation, we store 2D rectangular regions containing a ring artifact. These 2D fragments are transferred to several adjacent slices according to thickness distribution. It makes sense to store 3D regions containing rings and to do modification of statement (2) for taking account intensities from adjacent slices not just single slice. Because ring artifacts acquired by other microCT systems look slightly different, re-training of our 3D U-net might be required. The proposed procedure of dataset creation can help to create a general solution across the microCT systems of any manufacturer. Also, potentially, using different network architecture, for example, M-net [35] for more attention to fine details can provide better performance.

REFERENCES

- [1] T.M. Buzug, *Computed tomography: from photon statistics to modern cone-beam CT*. New York: Springer Science & Business Media, 2008.
- [2] I. Safonov, I. Yakimchuk, and V. Abashkin, "Algorithms for 3D Particles Characterization Using X-Ray Microtomography in Proppant Crush Test", *Journal of Imaging*, vol. 4(11), 2018, pp. 134.
- [3] I. Varfolomeev, I. Yakimchuk, and I. Safonov, "An Application of Deep Neural Networks for Segmentation of Microtomographic Images of Rock Samples", *Computers*, vol. 8(4), 2019, pp. 72.
- [4] C.F. Berg, O. Lopez, and H. Berland, "Industrial applications of digital rock technology", *Journal of Petroleum Science and Engineering*, vol. 157, 2017, pp. 131-147.
- [5] J.F. Barrett, and N. Keat, "Artifacts in CT: recognition and avoidance" *Radiographics*, vol. 24(6), 2004, pp. 1679-1691.
- [6] D. Prell, Y. Kyriakou, and W.A. Kalender, "Comparison of ring artifact correction methods for flat-detector CT", *Physics in Medicine & Biology*, vol. 54(12), 2009, pp. 3881.
- [7] J. Sijbers, and A. Postnov, "Reduction of ring artefacts in high resolution micro-CT reconstructions", *Physics in Medicine & Biology*, vol. 49(14), 2004 pp. N247.
- [8] M. Axelsson, S. Svensson, and G. Borgefors, "Reduction of ring artifacts in high resolution X-ray microtomography images", in *Joint Pattern Recognition Symposium*, 2006, pp. 61-70.
- [9] A. Lyckegaard, G. Johnson, and P. Tafforeau, "Correction of ring artifacts in X-ray tomographic images", *Int. J. Tomo. Stat.*, vol. 18, 2011, pp. 1-9.
- [10] E.M.A. Anas, J.G. Kim, S.Y. Lee, and M.K. Hasan, "Comparison of ring artifact removal methods using flat panel detector based CT images", *Biomedical engineering online*, vol. 10(1), 2011, pp. 72.
- [11] A. Telea, "An image inpainting technique based on the fast marching method", *Journal of graphics tools*, vol. 9(1), 2004, pp. 23-34.
- [12] C. Guillemot, and O. Le Meur, "Image inpainting: Overview and recent advances", *IEEE signal processing magazine*, vol. 31(1), 2013, pp. 127-144.
- [13] J. Xie, L. Xu, and E. Chen, "Image denoising and inpainting with deep neural networks", in *Advances in neural information processing systems*, 2012, pp. 341-349.
- [14] J. Yu, Z. Lin, J. Yang, X. Shen, X. Lu, and T.S. Huang, "Generative image inpainting with contextual attention", in *Proceedings of the IEEE conference on computer vision and pattern recognition*, 2018, pp. 5505-5514.
- [15] S. Iizuka, E. Simo-Serra, and H. Ishikawa, "Globally and locally consistent image completion", *ACM Transactions on Graphics (ToG)*, vol. 36(4), 2017, pp. 1-14.
- [16] C. Yang, X. Lu, Z. Lin, E. Shechtman, O. Wang, and H. Li, "High-resolution image inpainting using multi-scale neural patch synthesis", in *Proceedings of the IEEE Conference on Computer Vision and Pattern Recognition*, 2017, pp. 6721-6729.
- [17] G. Liu, F.A. Reda, K.J. Shih, T.C. Wang, A. Tao, and B. Catanzaro, "Image inpainting for irregular holes using partial convolutions", in *Proceedings of the European Conference on Computer Vision (ECCV)*, 2018, pp. 85-100.
- [18] Z. Yan, X. Li, M. Li, W. Zuo, and S. Shan, "Shift-net: Image inpainting via deep feature rearrangement", in *Proceedings of the European conference on computer vision (ECCV)*, 2018, pp. 1-17.
- [19] D. Ulyanov, A. Vedaldi, and V. Lempitsky, "Deep image prior", in *Proceedings of the IEEE Conference on Computer Vision and Pattern Recognition*, 2018, pp. 9446-9454.
- [20] S. Adiga, and J. Sivaswamy, "FPD-M-net: Fingerprint Image Denoising and Inpainting Using M-net Based Convolutional Neural Networks", in *Inpainting and Denoising Challenges*, 2019, pp. 51-61.
- [21] M. Unberath, J. Hajek, T. Geimer, F. Schebesch, M. Amrehn, and A. Maier, "Deep learning-bases inpainting for virtual DSA", in *IEEE Nuclear science symposium and medical imaging conference*, 2017, pp. 1-2.
- [22] H. Roy, S. Chaudhury, T. Yamasaki, D.M. DeLatta, M. Ohtake, and T. Hashimoto, "Lunar Surface Image Restoration Using U-Net Based Deep Neural Networks", in *Lunar and Planetary Science Conference*, Mar. 2019, vol. 50.
- [23] O. Ronneberger, P. Fischer, and T. Brox, "U-net: Convolutional networks for biomedical image segmentation" in *International Conference on Medical image computing and computer-assisted intervention*, 2015, pp. 234-241.
- [24] S. Chang, X. Chen, J. Duan, and X. Mou, "A hybrid ring artifact reduction algorithm based on CNN in CT images", in *15th International Meeting on Fully Three-Dimensional Image Reconstruction in Radiology and Nuclear Medicine*, May 2019, vol. 11072, p. 1107226.
- [25] B. Münch, P. Trtik, F. Marone, and M. Stampanoni, "Stripe and ring artifact removal with combined wavelet—Fourier filtering", *Optics express*, vol. 17(10), 2009, pp. 8567-8591.
- [26] C.H. McCollough, et al., "Low-dose CT for the detection and classification of metastatic liver lesions: Results of the 2016 Low Dose CT Grand Challenge", *Medical physics*, vol. 44(10), 2017, pp. e339-e352.
- [27] A. Kornilov, I. Safonov, and I. Yakimchuk, "Blind Quality Assessment for Slice of Microtomographic Image", in *2019 24th Conference of Open Innovations Association (FRUCT)*, 2019, pp. 170-178.
- [28] Ö. Çiçek, A. Abdulkadir, S.S. Lienkamp, T. Brox, and O. Ronneberger, "3D U-Net: learning dense volumetric segmentation from sparse annotation", in *International conference on medical image computing and computer-assisted intervention*, Oct. 2016, pp. 424-432.
- [29] Z. Wang, E.P. Simoncelli, and A.C. Bovik, "Multiscale structural similarity for image quality assessment", in *The Thirty-Seventh Asilomar Conference on Signals, Systems & Computers*, Nov. 2003, vol. 2, pp. 1398-1402.
- [30] H. Zhao, O. Gallo, I. Frosio, and J. Kautz, "Loss functions for image restoration with neural networks", *IEEE Transactions on computational imaging*, vol. 3(1), 2016, pp. 47-57.
- [31] D.P. Kingma, and J. Ba, "Adam: A method for stochastic optimization", in *Proceedings of the 3rd International Conference on Learning Representations*, 2014.
- [32] S. Athar, and Z. Wang, "A Comprehensive Performance Evaluation of Image Quality Assessment Algorithms", *IEEE Access*, vol. 7, 2019, pp. 140030-140070.
- [33] H.C. Shin, et al., "Deep convolutional neural networks for computer-aided detection: CNN architectures, dataset characteristics and transfer learning", *IEEE transactions on medical imaging*, vol. 35(5), 2016, pp. 1285-1298.
- [34] A. Paszke, et al., "Automatic differentiation in pytorch", *NIPS 2017 Workshop Autodiff*, 2017.
- [35] R. Mehta, and J. Sivaswamy, "M-net: A convolutional neural network for deep brain structure segmentation", in *2017 IEEE 14th International Symposium on Biomedical Imaging (ISBI 2017)*, Apr. 2017, pp. 437-440.